optica

Tailoring spatial entropy in extreme ultraviolet focused beams for multispectral ptychography

Lars Loetgering,[1,2,3,†] Xiaomeng Liu,[1,2,†] Anne C. C. De Beurs,[1,2] Mengqi Du,[1,2] Guido Kuijper,[2] Kjeld S. E. Eikema,[1,2] and Stefan Witte[1,2,*]

[1]Vrije Universiteit, De Boelelaan 1105, 1081 HV Amsterdam, The Netherlands
[2]Advanced Research Center for Nanolithography, Science Park 106, 1098 XG Amsterdam, The Netherlands
[3]e-mail: lars.loetgering@fulbrightmail.org
*Corresponding author: witte@arcnl.nl

Received 11 September 2020; revised 10 December 2020; accepted 10 December 2020 (Doc. ID 410007); published 25 January 2021

Diffractive optics can be used to accurately control optical wavefronts, even in situations where refractive components such as lenses are not available. For instance, conventional Fresnel zone plates (ZPs) enable focusing of monochromatic radiation. However, they lead to strong chromatic aberrations in multicolor operation. In this work, we propose the concept of spatial entropy minimization as a computational design principle for both mono- and polychromatic focusing optics. We show that spatial entropy minimization yields conventional ZPs for monochromatic radiation. For polychromatic radiation, we observe a previously unexplored class of diffractive optical elements, allowing for balanced spectral efficiency. We apply the proposed approach to the design of a binary ZP, tailored to multispectral focusing of extreme ultraviolet (EUV) radiation from a high-harmonic tabletop source. The polychromatic focusing properties of these ZPs are experimentally confirmed using ptychography. This work provides a new route towards polychromatic wavefront engineering at EUV and soft-x-ray wavelengths.

https://doi.org/10.1364/OPTICA.410007

1. INTRODUCTION

Microscopy with extreme ultraviolet (EUV) tabletop sources is a promising diagnostic tool for nanoscience but remains challenging due to the relatively low photon flux available as compared to large-scale facilities such as synchrotrons or free-electron lasers. In addition, focusing and shaping polychromatic EUV radiation using refractive optics such as lenses is intrinsically difficult, as most elements across the periodic table exhibit high absorption and low refractive index contrast in this spectral region. Alternative imaging approaches are therefore required. Full-field tabletop EUV microscopes employ Fresnel zone plates (ZPs) to directly image a specimen onto a detector [1,2]. Since the focal length of Fresnel ZPs is wavelength dependent, EUV full-field microscopes are typically restricted to monochromatic radiation. Although cascaded systems of diffractive optical elements (DOEs) with achromatic focusing capabilities have been reported [3,4], a monolithic approach is preferred for EUV radiation, where phase-shifting optical elements are hard to realize and thus binary DOEs with lower diffraction efficiency have to be used [5]. The requirement for monochromaticity results in a loss of rich chemical information that can be extracted from spectrally resolved refractive index studies [6]. A direction that has been followed more recently for EUV microscopy is coherent diffraction imaging (CDI) [7,8], which computationally recovers specimen information from a single diffraction intensity. While this technique has been applied for EUV tabletop microscopy, it works reliably only when information about the specimen, such as finite support or sparsity [9,10], is known *a priori*. CDI requires spatially coherent EUV radiation, which is available from tabletop setups through high-harmonic generation (HHG) [11–13]. HHG sources have the additional benefit of producing extremely broad EUV and soft-x-ray spectra, making them intrinsically suited for spectrally resolved microscopy. However, CDI requires monochromaticity, which principally limits its range of application for EUV microscopy, although some methods have been reported that relax this shortcoming through algorithmic extensions [14,15] or experimentally via spectrally resolved diffraction measurements [16]. Both full-field microscopy and CDI have a finite field of view limitation. Attempts have been reported to extend the field of view by using a compact scanning transmission microscope (STM) based on an HHG source [17]. However, in STM the lateral resolution is directly coupled to the beam size. In addition, the results in [17] were obtained with a multilayer mirror that limited the illumination to a single harmonic. Grazing incidence mirrors may be used to focus polychromatic radiation, but these typically suffer from low numerical apertures and are sensitive to misalignment [18]. Thus all the aforementioned techniques lack spectral sensitivity and involve a compromise between field of view and resolution. A promising technique to solve these challenges is ptychography [19,20], a combination of STM and CDI. Ptychography enables simultaneous wavefront sensing and quantitative phase contrast

microscopy at theoretically unlimited field of view [21–23]. Additionally, ptychography decouples spatial resolution from the illumination spot size. The large amount of information available in ptychography makes it possible to decode polychromatic wavefronts using only monochromatic detectors [24,25]. This is particularly useful for EUV microscopy, where polychromatic operation offers increased flux and enables chemical sensitivity, but wavelength-resolving cameras are not available. Most HHG-based ptychography applications to date have used multilayer mirrors that filtered the source spectrum to quasi-monochromatic radiation [22,26–30], and to our knowledge only a single result on multispectral EUV ptychography has been reported [31]. In the latter reference, the authors demonstrated the use of an ellipsoidal mirror in grazing incidence to produce a polychromatic focused beam. This approach is flux efficient, but it does not allow control over the structure of the incoming beam, which can be of great importance for reconstruction quality [32–35]. Here we demonstrate multispectral ptychography using structured EUV beams. To this end, we address the sub-problem of designing DOEs that are suitable for both confining and structuring polychromatic EUV radiation. This goal is achieved through a novel computational design principle based on spatial entropy minimization. While the designs reported in this paper are tailored to EUV radiation, the underlying concept may be used for both refractive and diffractive optics design in other spectral domains. In the first part of the paper, we introduce spatial entropy minimization, which formulates diffractive focusing as an optimization problem. It is shown that the approach generates conventional ZPs in the limit of monochromatic radiation. A wider class of designs is examined for polychromatic radiation, with the ability to balance spectral flux. In the second part, we report experimental results for multispectral EUV ptychography, where we apply entropy optimization to generate structured and focused beams. The proposed approach paves the way for utilizing the full potential of HHG sources for spectrally resolved EUV microscopy.

2. SPATIAL ENTROPY MINIMIZATION

Designing a multispectral ZP consists of two main ingredients, which we shortly summarize before proceeding to the mathematical formulation: First, polychromatic radiation needs to be confined into a preferably small focus. As detailed below, this constraint may be imposed by requiring the side lobes of the focal spot to decay with increasing distance from the optical axis. However, for the case of binary ZPs, we cannot prevent the presence of a zeroth-order diffraction contribution. Hence, the first constraint is enforced only inside the geometrical shadow of a central stop of the ZP, which is the interior of the purple circle in Fig. 1. In the final experiment, portions of the beam far away from the optical axis may be clipped using an order sorting aperture (OSA) complementary to the target focal plane region to suppress the zeroth order. Second, the ZP is required to be binary. This property facilitates nanofabrication and reduces losses due to absorption when used in transmission.

With regard to the first requirement, we consider the spatial entropy functional

$$\mathcal{S}[\psi_k(\boldsymbol{x})] = -\sum_{\boldsymbol{x}} A(\boldsymbol{x}) I(\boldsymbol{x}) \log I(\boldsymbol{x}), \tag{1}$$

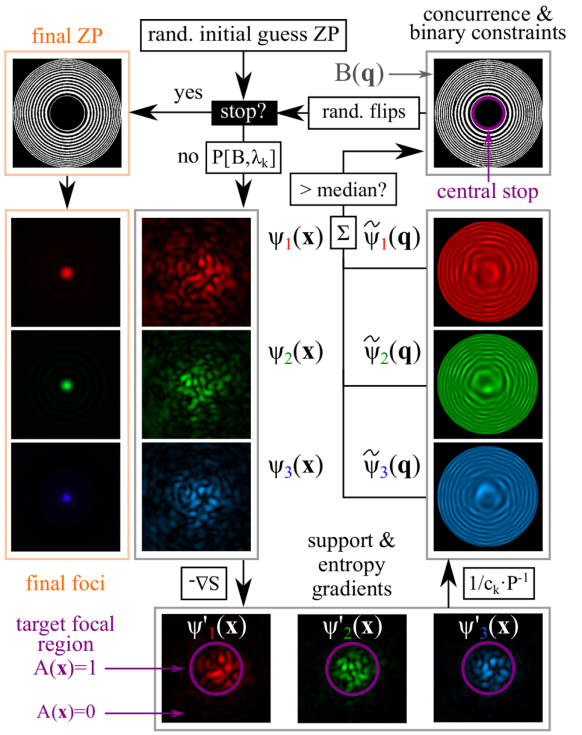

Fig. 1. ZP optimization. Starting at a suboptimal binary ZP initial guess, the focal spot distribution for each spectral wavefront is calculated, where a gradient step towards minimum spatial entropy and support is applied. The updated beams are backpropagated into the ZP plane, where spectral holograms are combined into a single ZP via the concurrence and binary constraints. A subset of the ZP pixels are randomly flipped to prevent stagnation in local minima before the next iteration starts. The violet circles in the top and lower part of the figure depict the beam and central stop supports in the focal and ZP planes, respectively.

where the summation is over all pixels with nonzero intensity in the focal plane. We assume the focal plane intensity $I(\boldsymbol{x}) = \sum_k \psi_k^*(\boldsymbol{x})\psi_k(\boldsymbol{x})$ to be the incoherent sum over all spectral field contributions $\psi_k(\boldsymbol{x})$ $(k = 1, \ldots, K)$ at wavelengths λ_k. The variable $\boldsymbol{x}$ denotes focal plane coordinates, and $A(\boldsymbol{x})$ is a binary function that is unity inside the geometrical shadow of the ZP central stop and zero elsewhere. Constraining the focused beam inside this finite domain in the target focal region leaves the zeroth order widely unaffected. Throughout this paper we normalize the intensity inside the focal plane

$$\sum_{\boldsymbol{x}} A(\boldsymbol{x}) I(\boldsymbol{x}) = 1 \tag{2}$$

when evaluating Eq. (1) to make the quoted entropy values (as in Table 1) independent of flux. We use the natural logarithm in Eq. (1); any other basis scales the entropy by a constant factor and does not affect the results. With these definitions, we make three observations: (i) $\mathcal{S}$ is non-negative. (ii) Minimum entropy is achieved when the normalized total intensity [cf. Eq. (2)] is concentrated in a single pixel, corresponding to an optimally focused beam. In this case $\mathcal{S} = 0$. (iii) Maximum entropy occurs when all pixels in the target domain have equal intensity. The first and second property directly follow as a result of the normalization in Eq. (2) and the logarithm evaluating negative for arguments $0 < I(\boldsymbol{x}) < 1$. A proof of the third property is provided in [36].

Table 1. Simulation Parameters for the ZP Optimization Results in Fig. 2[a]

Panel	$\langle\eta\rangle$	S_{final}	λ [nm]	% rand. flips	∇S
(a–c)	9.65%	11.71	47.1	25%–0%	✓
(d–f)	4.68%	12.54	34.8–47.1	5%–0%	✓
(g–i)	3.96%	12.63	34.8–47.1	25%–0%	—
(j–l)	4.54%	12.53	34.8–47.1	25%–0%	✓

[a]For each ZP we show the average spectral efficiency, the final spatial entropy, the wavelength range, the percentrage of random flips during annealing, and whether or not the entropy gradient was applied in the focal plane.

Together, these properties motivate us to use spatial entropy as a focusing measure.

Next, we consider a strategy that minimizes the entropy functional in Eq. (1). The complex gradient [37] of Eq. (1) with respect to ψ_k is given by

$$\frac{\partial \mathcal{S}}{\partial \psi_k^*(\boldsymbol{x})} = -A(\boldsymbol{x})\psi_k(\boldsymbol{x})(1+\log I(\boldsymbol{x})). \tag{3}$$

We minimize Eq. (1) using a gradient descent iterative update

$$\psi_k'(\boldsymbol{x}) = \psi_k(\boldsymbol{x}) - \alpha \frac{\partial \mathcal{S}}{\partial \psi_k^*(\boldsymbol{x})}, \tag{4}$$

where the parameter α may be adjusted to control the step size along the search direction. Equation (4) forces the spectral beam estimates towards minimum spatial entropy inside the target focal region where $A(\boldsymbol{x}) = 1$. We refer to Eq. (4) as the *minimum entropy update step*.

To calculate the required ZP, we define the spectrally summed hologram

$$H(\boldsymbol{q}) = \sum_k |\tilde{\psi}_k(\boldsymbol{q}) + \max|\tilde{\psi}_k(\boldsymbol{q})||^2, \tag{5}$$

where

$$\tilde{\psi}_k(\boldsymbol{q}) = \frac{1}{c_k}\mathcal{P}^{-1}[\psi_k'(\boldsymbol{x}), \lambda_k] \tag{6}$$

are the reweighted focal plane spectral fields backpropagated into the ZP plane with coordinates $\boldsymbol{q}$. Each $\mathcal{P}[\ldots, \lambda_k]$ is a bandlimited angular spectrum propagator at the respective wavelength λ_k [38]. The weights c_k, given by

$$c_k^2 = \sum_{\boldsymbol{x}} A(\boldsymbol{x})|\psi'_k(\boldsymbol{x})|^2, \tag{7}$$

are used to equalize the relative strength of the spectral intensities in the target focal region. Other choices may be used if unbalanced spectra are desired in the focal plane. The $\max|\tilde{\psi}_k(\boldsymbol{q})|$ term in Eq. (5) acts as a plane holographic reference with amplitude scaled to the maximum of each respective spectral field. We want the ZP to consist of either fully transmissive or opaque features. Therefore, we rewrite $H(\boldsymbol{q})$ as a binary ZP pattern according to

$$B(\boldsymbol{q}) = \begin{cases} 1, & H(\boldsymbol{q}) > \text{median}\,[H(\boldsymbol{q})] \\ 0, & \text{else} \end{cases}. \tag{8}$$

The comparison with the median constrains the number of transmissive and opaque elements of the ZP to be equal. We refer to Eqs. (5) and (8) as the *concurrence* and *binary constraints*, respectively. During the search process a small subset of pixels in $B(\boldsymbol{q})$ is randomly selected and flipped from 0 to 1 and vice versa. We denote the binary ZP resulting from the latter step by $B'(\boldsymbol{q})$. The number of random flips is gradually annealed to zero (see details below). The simulations presented in the next section indicate that random flips help prevent stagnation around the local minima of Eq. (1). As a final step, the updated focal plane spectral fields are given by

$$\psi_k''(\boldsymbol{x}) = \mathcal{P}[B'(\boldsymbol{q}), \lambda_k]. \tag{9}$$

After setting $\psi_k(\boldsymbol{x}) \leftarrow \psi_k''(\boldsymbol{x})$, the algorithm iterates through Eqs. (4)–(9) and stops when no progress in Eq. (1) is made towards lower entropy or when a predefined number of iterations is reached.

3. SIMULATION

We performed simulations of the entropy minimization algorithm proposed above and examined the influence of the source spectrum, the role of the entropy gradient, and the number of random flips following the concurrence and binary constraints. In each simulation we fixed the ZP diameter to $D = 159$ μm, the smallest feature size to $\Delta x = 310$ nm, and the focal length to $f = 4.9$ mm, assuming radiation from an HHG source with a fundamental driving laser wavelength of 800 nm upconverted to the 17th to 23rd harmonic (34.8 nm to 47.1 nm). All values listed above were chosen similar to the experimental parameters below. We note that the feature size is defined here as the smallest spatial scale over which the ZP can switch from opaque to transmissive and vice versa. The bandlimited angular spectrum propagator $\mathcal{P}$ assumes the same pixel size in the zone plate and focal plane. All simulations below are performed with

$$A(\boldsymbol{x}) = \begin{cases} 1, & \|\boldsymbol{x}\| < 5\ \mu\text{m} \\ 0, & \text{else} \end{cases} \tag{10}$$

and $\alpha = 0.25$ [compare Eq. (4)]. The spectral beam size σ_k is defined here via the truncated second moment

$$\sigma_k^2 = \frac{\sum_{\boldsymbol{x}} \boldsymbol{x}^2 A(\boldsymbol{x})|\psi_k(\boldsymbol{x})|^2}{\sum_{\boldsymbol{x}} A(\boldsymbol{x})|\psi_k(\boldsymbol{x})|^2}, \tag{11}$$

where $A(\boldsymbol{x})$ is used to mask out zero-order contributions beyond the target focal region. The average beam size is the arithmetic mean over all spectral beam sizes in the focal plane

$$\langle\sigma\rangle = \frac{1}{\Lambda}\sum_k \sigma_k, \tag{12}$$

where Λ is the number of spectral lines. The spectral efficiency is defined here as the ratio of the energy in the target focal region divided by the energy incident on the circular area containing the ZP, evaluated separately at each wavelength λ_k:

$$\eta_k[B] = \frac{4}{\pi D^2}\sum_{\boldsymbol{x}} A(\boldsymbol{x})|\psi_k(\boldsymbol{x})|^2\Delta x^2, \tag{13}$$

where D is the ZP diameter and we assume the ZP is illuminated by a plane wave of unit intensity at every pixel and wavelength.

Figure 2(a) shows in the upper left corner the entropy minimization result (white) for only the 17th harmonic present in the spectrum incident on the ZP. The fraction of random flips

in the allowed ZP area, limited by the fixed ZP diameter and the central stop, was linearly annealed from 25% to 0% within a total of 1000 iterations. A standard ZP characterized by two parameters, namely, the wavenumber κ and a constant phase offset ϕ, was fit to the output of the entropy minimization algorithm by solving the nonlinear least-squares problem:

$$\underset{\kappa,\phi}{\operatorname{argmin}} \sum_{\boldsymbol{q}} w(\boldsymbol{q})\left(B(\boldsymbol{q}) - \operatorname{sgn}\left[\cos\left(\kappa\sqrt{f+\boldsymbol{q}^2}+\phi\right)\right]\right)^2. \tag{14}$$

For the simulations in this section, the weighting function $w(\boldsymbol{x})$ is given by

$$w(\boldsymbol{q}) = \begin{cases} 1, & 10\ \mu\text{m} < \|\boldsymbol{q}\| < 79.5\ \mu\text{m} \\ 0, & \text{else} \end{cases} \tag{15}$$

to account only for the pixels inside the outer diameter (159 μm) and outside the central stop diameter (20 μm) of the ZP. We note that the central stop diameter is chosen to be larger than the target focal plane diameter (10 μm) to reduce the contribution of the zeroth order in the target focal plane. The ZP fit to the output of the monochromatic minimum entropy ZP is shown in the lower right corner (turquoise) of Fig. 2(a), where the violet inset highlights the match for the outermost zones. Here the fitting parameters are $\kappa = 0.1335\ \text{nm}^{-1}$ and $\phi = 0.5587$ rad. A lateral cross section of the focused beam in the target focal plane is shown in Fig. 2(b). Here, and in all other panels in the middle and bottom rows of Fig. 2, the color coding indicates the wavelengths from long to short, namely, red (17th harmonic, $\lambda_1 = 47.1$ nm), yellow (19th harmonic, $\lambda_2 = 42.1$ nm), green (21st harmonic, $\lambda_3 = 38.1$ nm), and blue (23rd harmonic, $\lambda_4 = 34.8$ nm). The monochromatic and average beam sizes are indicated by σ and $\langle\sigma\rangle$, respectively, according to Eqs. (11) and (12). In Fig. 2(c), we plot the evolution of the spatial entropy functional $\mathcal{S}[\psi_k]$ of the beam in the focal plane (black, left vertical axis) and the spectral efficiency $\eta_k[B]$ (red, right vertical axis) of the ZP design versus iteration number. The minimum entropy solution for the monochromatic case results in a conventional binary ZP reaching a final efficiency of 9.65%. Due to losses introduced by the central stop [35], this is slightly lower than the theoretical maximum for a conventional, binary ZP of $1/\pi^2 \approx 10.13\%$ [5]. We conclude that our entropy minimization approach results in conventional ZPs for monochromatic radiation. In Figs. 2(d)–2(f) we assumed all four harmonics (17th to 23rd) to be present in the incident beam. We first study the role of the number of random flips in the design. Here the fraction of random flips in the allowed ZP area was linearly annealed from 5% to 0% within 1000 iterations, instead of 25% to 0% as done in all other simulations reported in this section. Similar to the monochromatic case, Fig. 2(f) shows the efficiencies of the spectral intensities (red, yellow, green, and blue; y axis on the right) increase as the spatial entropy (black; left y axis) is minimized. The formation of asymmetries, such as pitchfork-shaped bifurcations in Fig. 2(d), suggests the algorithm found a suboptimal result, as there should not be a preferred direction in the solution of the problem. The individual spectral efficiencies in the target focal region are found to be $\eta_1 = 3.55\%$, $\eta_2 = 4.85\%$, $\eta_3 = 5.34\%$, and $\eta_4 = 4.98\%$, resulting in an average spectral efficiency of ($\langle\eta\rangle = 4.68\%$). In Figs. 2(g)–2(i) we investigated the effect of not

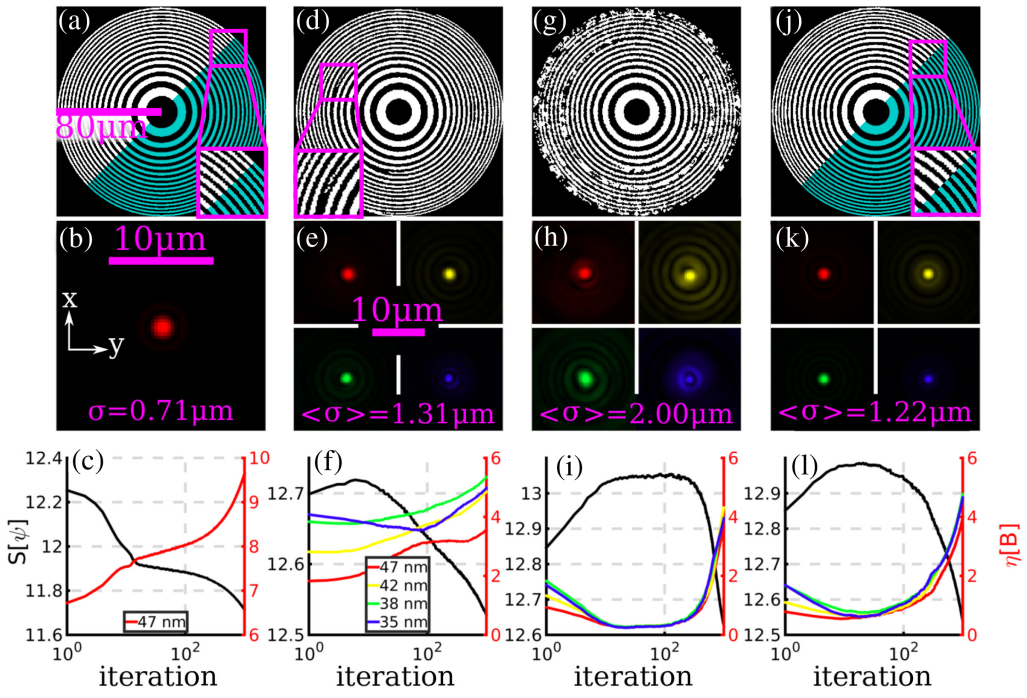

Fig. 2. Simulated ZP designs. (a) Monochromatic spatial entropy minimization zone plate estimate. The violet inset in (a) indicates a match out to the smallest zones between the optimized ZP (white) and a conventional ZP with fitted parameters (turquoise). (b) The monochromatic focal plane intensity cross section corresponding to the ZP estimate in (a). (c) Entropy (black) and efficiency (red) versus iteration (1000 iterations, logarithmic scale). (d) Optimization result for multicolor ZP with a small percentage (5%) of random flips. (e) Focal plane intensity cross sections for four different harmonic wavelengths. (f) Entropy (black) and efficiency for all four wavelengths. (g)–(i) Multicolor ZP with 25% of random flips and entropy gradient switched off. (j)–(l) Multicolor ZP with 25% of random flips and entropy gradient switched on. The solution in (j) cannot be fit to a conventional ZP. In the bottom row we compare the focal plane entropy (black line, left vertical axis) and the focal plane beam spectral efficiencies (colored lines, right vertical axis) for each respective ZP. The scale bars are shared throughout each row. The parameters for this simulation are summarized in Table 1.

making use of the entropy gradient and only imposing a support constraint, pushing the tails of the focal plane spectral beams to zero outside the target region. This is achieved by neglecting the log term in Eq. (3). In this case, the algorithm settled for a suboptimal result, qualitatively indicated by the large number of asymmetries in both the final ZP [Fig. 2(g)] and the focal plane beam intensities [Fig. 2(h)], and quantitatively expressed by the lower average spectral efficiency ($\langle\eta\rangle = 3.96\%$) in Fig. 2(i) as compared to the previous and following case. This underlines the importance of the entropy gradient in finding a ZP for multispectral operation. In Figs. 2(j)–2(l) we repeated the simulation with identical parameters as in Figs. 2(d)–2(f) but annealed the fraction of random flips in the ZP from initially 25% to a final 0%. In this case, a highly symmetric solution was found, which resulted in the lowest spatial entropy in the focal plane among the polychromatic cases tested (see Visualization 1 and Visualization 2). This shows that the number of random flips is crucial in allowing the algorithm to escape local minima in the entropy functional. We attempted to fit a conventional ZP [turquoise in Fig. 2(j)] to the output (white) of the entropy minimization algorithm for the polychromatic focusing problem (best fit parameters: $\kappa = 0.1655\,\mathrm{nm}^{-1}$ and $\phi = 3.4795$ rad). The mismatch in the violet inset shows that the aforementioned parameters cannot model the output of the ZP estimate for the polychromatic focusing underlying Fig. 2(j), in contrast to the ZP estimate for the monochromatic focusing problem in Fig. 2(a). The conventional ZP fit (turquoise) yields highly unbalanced spectral efficiencies $\eta_1 = 0.90\%$, $\eta_2 = 3.96\%$, $\eta_3 = 9.77\%$, and $\eta_4 = 6.96\%$ ($\langle\eta\rangle = 5.39\%$). Although the average efficiency performs better than our entropy minimization designs, the efficiencies in the target focal region for the 17th and 21st harmonics are an order of magnitude apart, rendering conventional ZPs poor candidates for multispectral operation. In contrast, the result of our entropy minimization algorithm exhibits a good balance in the spectral efficiencies $\eta_1 = 3.98\%$, $\eta_2 = 4.73\%$, $\eta_3 = 4.77\%$, and $\eta_4 = 4.65\%$ ($\langle\eta\rangle = 4.54\%$), making them more applicable for operation at multiple wavelengths than conventional ZPs. The most relevant parameters of the simulations in this section are summarized in Table 1.

Further insight into the flux balancing mechanism provided by entropy minimization is obtained by examining the resulting axial beam cross sections around the focal plane. In Fig. 3 we compare axial beam cross sections obtained from the conventional ZP in Fig. 2(a) and the minimum entropy ZP in Fig. 2(j), both in polychromatic operation. The left column of Fig. 3 shows the focusing behavior of the conventional ZP. It is seen that a wavelength shift causes an axial displacement of the focal plane. This axial displacement is an immediate consequence of the exchangeable roles that the wavelength and the propagation distance play in paraxial diffraction [39]. The flux in a single observation plane (semitransparent line) is widely unbalanced as a result of the beam being dominated by a single diffraction order. The right column of Fig. 3 shows the focusing behavior of the ZP optimized for minimum entropy from Fig. 2(j). It is seen that the entropy minimization approach yields multiple and more balanced diffraction orders as compared to the conventional ZP. Changing the wavelength results in an axial displacement of the minimum entropy beam. However, for the minimum entropy beam the diffraction orders coincide upon axial displacement, in contrast to the beam generated from the conventional ZP. We conclude that entropy minimization achieves flux balancing through axial alignment of higher diffraction orders.

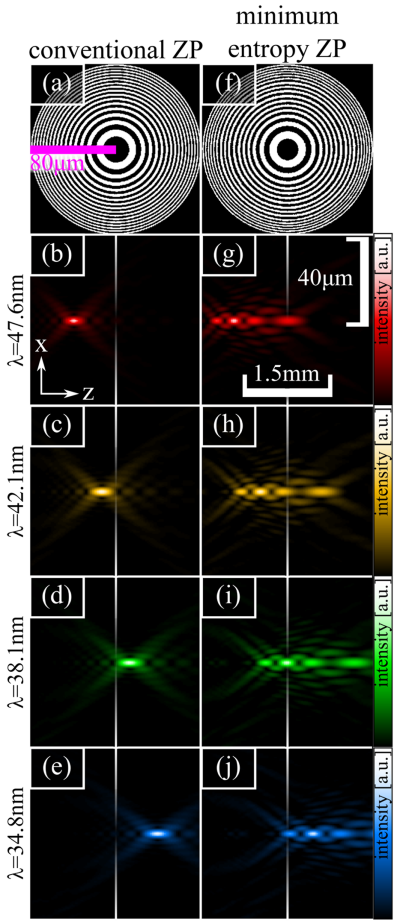

Fig. 3. Simulated axial cross sections of conventional (left) and minimum entropy (right) ZPs. Conventional ZPs concentrate most flux into a single diffraction order while minimum entropy ZPs distribute the flux among multiple orders. In both cases wavelength modifications cause an axial displacement of the beam around the focal plane. In contrast to conventional ZPs, the minimum entropy ZP exhibits balanced diffraction orders which coincide upon axial displacement. In panels (b)–(e) and (g)–(j) the semitransparent lines serve as reference to compare the axial location of the diffraction orders.

Two final notes concern the uniqueness of the simulation results and computational complexity: First, we have constrained the algorithm to focus into a relatively large target focal region with a diameter of 10 μm. However, the entropy minimization algorithm gives a solution with significantly smaller beam size. If the target focal region is constrained to be circular as given in Eq. (10), the entropy functional in Eq. (1) is invariant under translation of the focal spot intensity and the solution is nonunique. In particular, this can result in ZPs with off-axis focus. Practically, we omitted this by choosing a smooth apodization function

$$A(\boldsymbol{x}) = \exp\left(-\frac{\boldsymbol{x}^2}{2\sigma^2}\right), \tag{16}$$

with a full width at half-maximum of $\mathrm{FWHM} = 2\sqrt{2\ln(2)}\sigma = 10$ μm. This was used only for the entropy update step [Eq. (4)], while the renormalization step [Eq. (7)] and the evaluation of spectral efficiency [Eq. (13)] used the circular apodization function described by Eq. (10). Second, the computational complexity of a single iteration of the entropy minimization algorithm scales with $\mathcal{O}[\Lambda \cdot P \cdot \log P]$, where P is the total number of pixels in

the ZP. Each ZP optimization described in this section ($P = 2^{20}$, $\Lambda = 4$, 10^3 iterations) required 160 s using GPU-accelerated computation on a NVIDIA Tesla K40 and a MATLAB software implementation.

4. EXPERIMENTAL RESULTS

A. Zone Plate Design Considerations for EUV Ptychography

In this section we summarize considerations to match free parameters in the minimum entropy ZP design for operation in our EUV ptychography setup. We start with the diameter of the target focal plane. While the object field of view in monochromatic far-field ptychography is theoretically unlimited through transverse scanning, the probe field of view (pFOV) is restricted by the experimental geometry:

$$\mathrm{pFOV} = \frac{\lambda z}{b \Delta u}, \tag{17}$$

where Δu is the detector pixel size, b is the binning factor, and z is the sample-detector distance [39]. In polychromatic ptychography, Eq. (17) is a function of wavelength, with the most restricted pFOV found at the minimum wavelength in the probe spectrum. Under optimized conditions for HHG in argon using an 800 nm driving laser, our source provides appreciable flux down to $\lambda_{\mathrm{min}} = 25$ nm. For a sample-detector distance of $z = 90$ mm, dictated by the geometry of our experimental vacuum chamber, and a binning factor of $b = 4$ (to reduce the computational overhead of the Fourier transforms involved in the multispectral ptychography solver, see Section 4.B below), this results in a minimum pFOV of 41.6 μm. We achieve an oversampling ratio better than 2 per dimension [40] by restricting the target focal region to 15 μm.

Another important consideration is the desired beam shape. We demonstrated above that minimum entropy ZPs can be designed for multispectral operation. However, they are not necessarily optimal for ptychography, which benefits from spatially extended and structured beams [32–35]. While this has previously been shown for monochromatic radiation, the same observation holds for polychromatic ptychography (see Supplement 1). We thus decided to find a compromise between the need for probe localization as dictated by Eq. (17) (which is achieved by entropy minimization) and introducing spectrally dependent spatial structure into the polychromatic wavefront. Revisiting the simulation results in Figs. 2(d)–2(f) and the corresponding row in Table 1, we see that aberrations caused by the presence of bifurcations in the ZP design can introduce structure into the illumination while still providing a fair balance between the energy of each spectral field in the focal plane [35]. Our final ZP design was optimized using entropy minimization for six harmonics (the 17th to 27th order) simultaneously. We note that annealing with only 0.5%–0% random flips was used to promote the formation of bifurcations in the ZP, while searching for a solution with low entropy. Based on this a ZP was manufactured with additional support structure as shown in Fig. 4(a). The ZP has an outer diameter of 240 μm, a smallest feature size of 155 nm, and a focal distance of 4.2 mm. A central stop with a diameter of 75 μm was left opaque. This region can be used in conjunction with an order-sorting aperture of the same size to block the undiffracted portion of the radiation transmitted through the ZP. Our simulations indicate that the ZP has an estimated average spectral efficiency of better than 3%.

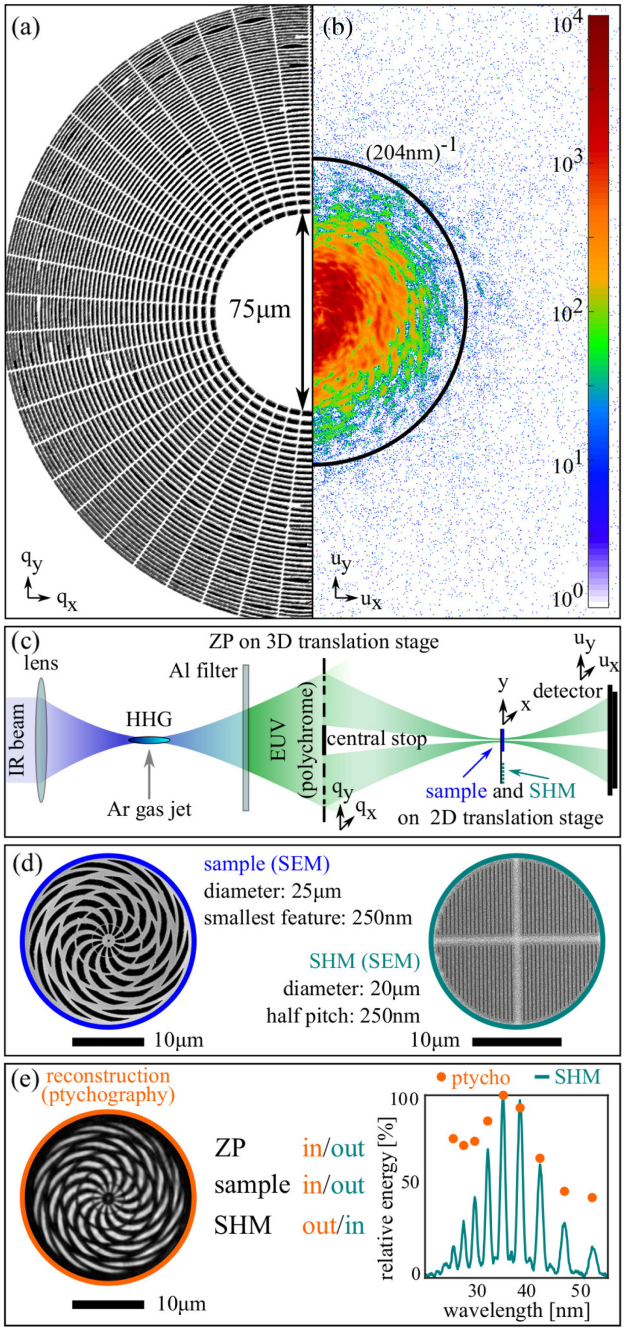

Fig. 4. (a) SEM image of ZP. (b) Experimental diffraction pattern produced by illuminating the sample shown in (d) using the ZP shown in (a). (c) Experimental setup. A fundamental infrared (IR) beam is focused into an argon (Ar) gas jet resulting in high-harmonic generation (HHG). After the IR beam (blue) is blocked by an aluminium (Al) filter, a binary ZP focuses the polychromatic EUV (green) beam onto a sample (d) mounted on a translation stage. A spectral Hartmann mask (SHM) [41], consisting of 21 grating apertures, like the one shown in (d), can be moved into the beam with the ZP removed to identify the spectral lines in the HHG spectrum (see panel e). (e) Ptychographic reconstruction of sample (left) and reconstructed (orange) versus measured (turquoise) spectrum (right).

B. Nanofabrication

The multicolor binary ZP as described in the previous subsection was fabricated on a 90 nm thick Au layer sputter coated on a 50 nm thick Si_3N_4 membrane (Ted Pella Inc.). The pattern was milled with a 30 keV focused gallium ion beam (FEI Helios Nanolab

600). The ion-beam current was set to 48 pA with a focal spot diameter of 50 nm. The ZP was milled in 12 cycles with a sputter step size of 35 nm and dwell time of 60 ms. The total time required for nanofabrication was approximately 6 h. In addition, we fabricated a binary sample for wavefront analysis of the multispectral wavefront produced by the ZP. Periodic structures were initially taken into consideration. However, periodic samples are not ideal for ptychography, as they give rise to localized diffraction peaks. These saturate a few detector pixels quickly while leaving others at a low level of exposure, allowing only a small total number of photons to be recorded. Moreover, self-calibration methods such as lateral position correction are challenging [42]. Hence we designed a sample [see Fig. 4(d) left side] that is aperiodic upon lateral translation. An analytical expression for the sample transmission function is given by

$$O(\rho,\theta)=\frac{1}{2}\left(1+\operatorname{sgn}\left[\sin\left(a\theta+2\pi\left(\frac{\rho}{b}\right)^2\right)\right]\right)t(\rho), \quad (18)$$

where (ρ,θ) are polar coordinates,

$$t(\rho)=\operatorname{rect}\left(\frac{\rho}{d_1}\right)\cdot\left[1-\operatorname{rect}\left(\frac{\rho}{d_2}\right)\right]+\operatorname{rect}\left(\frac{\rho}{d_3}\right), \quad (19)$$

and

$$\operatorname{rect}(\rho)=\begin{cases}1, & \rho\le 1/2\\ 0, & \text{else.}\end{cases} \quad (20)$$

$t(\rho)$ is an apodization function that guarantees each spectral wavefront downstream of the sample is oversampled according to Eq. (17). This is a useful property when reconstructing strongly defocused beams. The free parameters in the first term in Eq. (18) allow us to control the number ($a=13$) and the curvature of the spokes ($b=5$ μm). The free parameters in the apodization function control the outer (d_1) and inner diameter (d_2) of the object. Stabilizing support rings and a dot were added at the center with a diameter (d_3) close to the lateral resolution limit at the central wavelength our ptychography setup (214 nm full period at 32 nm). These parameters were chosen as $d_1=25$ μm, $d_2=2$ μm, and $d_3=250$ nm. An SEM image of the final sample is shown in Fig. 4(d).

C. Experimental Setup

The EUV measurements have been carried out using a tabletop HHG source. A noncollinear optical chirped-pulse amplifier system amplifies infrared pulses with a central wavelength of 800 nm generated by a Ti:sapphire oscillator. This system delivers driving pulses with a duration of 25 fs at a repetition rate of 300 Hz. A pulse energy of 2 mJ is typically used for HHG. These pulses are focused into an argon (Ar) gas jet and are upconverted to EUV wavelengths through the HHG process as illustrated in Fig. 4(c). An aluminum (Al) membrane with a thickness of 200 nm is used to filter out the fundamental beam while the HHG beam is transmitted. This EUV beam is focused by the ZP onto a sample, which is mounted on a two-dimensional translation stage (Smaract SLC-1730) required to perform ptychography scans. In addition, a spectral Hartmann mask (SHM) is mounted next to the sample [41]. The SHM consists of multiple apertures with gratings inscribed, one of which is shown in Fig. 4(d). We note that the SHM cannot be used for wavefront sensing on focused beams and is used here only for the characterization of the HHG spectrum with the ZP removed from the beam path. The identified spectral lines, but not their relative weights, are used in the ptychography algorithm below as prior knowledge. Finally, a CCD camera (Andor Ikon-L 936 SO, 2048x2048 pixels, pixel size 13.5 μm) collects diffraction patterns at a distance of 92.5 mm downstream of the specimen and SHM. A typical multiwavelength HHG diffraction pattern with the described setup is shown in Fig. 4(b).

D. Multispectral Ptychography

Our reconstruction algorithm is based on ptychographic information multiplexing [24], which models the observed intensity on the monochromatic detector as an incoherent sum of multiple monochromatic diffraction patterns. All algorithmic details are given in Supplement 1. We collected a ptychographic scan consisting of 252 scan positions covering a field of view with a diameter of 50 μm. The average scan step was 2.5 μm, and the diameter of the binary object is 25 μm, resulting in a linear overlap of approximately 90% [43]. This relatively high degree of overlap in scan positions enabled us to reconstruct the spatial structure and the spectral weights of the beam. In Figs. 5(a1)–5(i1) we show the simulated beam assuming the ZP design from Fig. 4(a) under plane wave illumination. In Fig. 4(e) and in Figs. 5(a2)–5(i2) we show the ptychographic reconstruction of the object and the spectral beam profiles, respectively. We find good qualitative agreement between simulation, as shown in Figs. 5(a1)–5(i1), and experiment, in particular for the central harmonics. The largest discrepancy is observed at the extremal spectral lines, where the signal-to-noise ratio is lowest and defocusing is most severe. Moreover, differences between the simulated and the reconstructed beam profiles arise from fabrication errors in the ZP as seen in Fig. 4(a). In addition, the spectral wavefronts illuminating the ZP are not perfectly planar. In Figs. 5(a3)–5(i3) we show each spectral beam intensity integrated along the y direction at ±500 μm around the focal plane. This projected view is adopted here due to the lack of centrosymmetry in the beam.

Figure 4(e) shows the relative energy of the reconstructed beam (orange dots) as compared to the spectrum extracted using the SHM (turquoise line). We note that the spectrum measured by the SHM is acquired without ZP in the beam. Thus, the spectra obtained from the SHM are not expected to match in the weights of the spectral lines estimated by ptychography. It is emphasized that no *a priori* knowledge was used to obtain the spectral weights during the reconstruction process. This is possible because the object is binary (ptychographic reconstruction shown in Fig. 4(e), left). In cases where the object is dispersive, modulating each spectral wavefront in a different way, additional information about the source spectrum is required [24].

5. DISCUSSION AND CONCLUSION

In summary, we proposed a new route to polychromatic focusing based on spatial entropy minimization, enabling flux balancing in the design of polychromatic focusing optics. The ability to efficiently shape and focus the polychromatic flux offered by HHG sources is a key challenge in the realization of spectrally resolved tabletop EUV microscopes in the near future. Our proof-of-concept experiments demonstrate multispectral focusing and wavefront shaping are possible with binary DOEs, which were previously not considered for tabletop ptychographic scanning

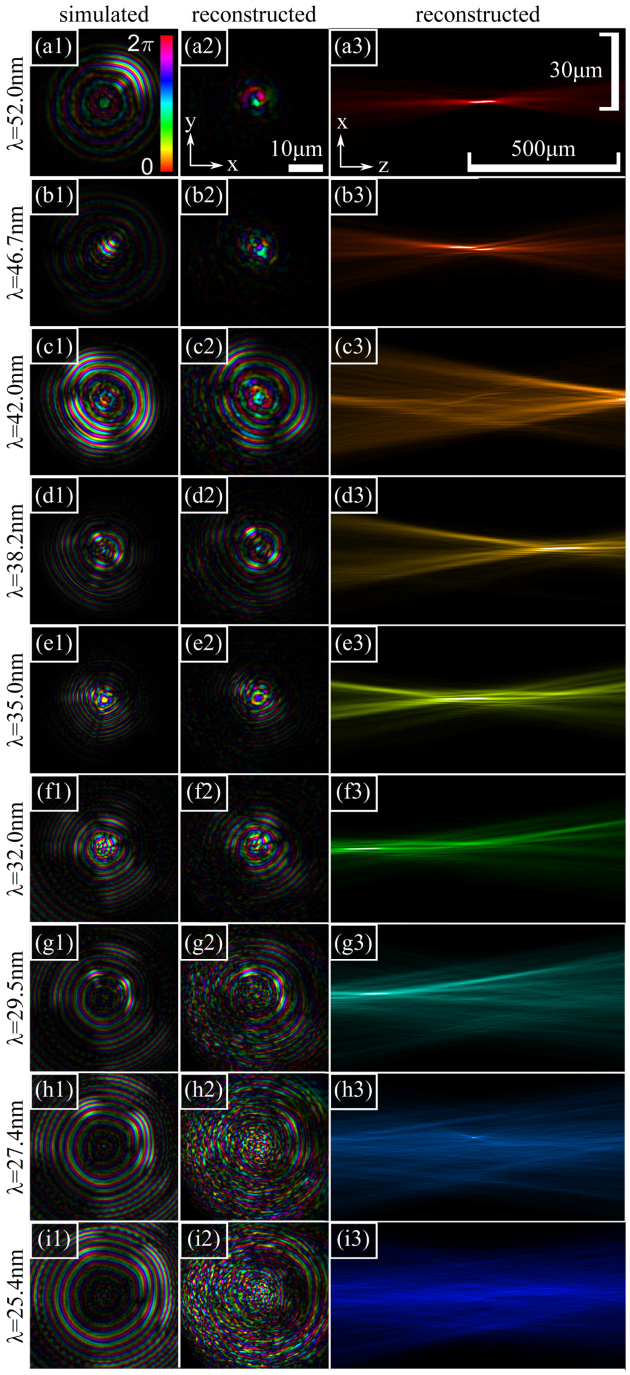

Fig. 5. Left column: lateral $(x-y)$ cross sections of simulated spectral beam profiles (a1)–(i1) assuming the ZP design in Fig. 4(a). Middle column: lateral $(x-y)$ cross sections of ptychographic spectral beam reconstructions (a2)–(i2). The scale bar in panel (a2) depicts the extent of the focal plane support and is shared among the first two columns. Right column: axial $(x-z)$ cross sections (a3)–(i3). The scale bars along the horizontal and vertical directions have different scaling and are shared among the third column. The left and middle columns represent complex beam profiles, where amplitude and phase are encoded as brightness and hue, respectively. The right column depicts intensity linearly encoded as brightness, and color encodes wavelength.

microscopes. Furthermore, we show that multispectral ptychography is capable of reconstructing a multitude of complex-shaped EUV field distributions in parallel and thus provide a method that can effectively use the generated wavefronts for spectrally resolved high-resolution imaging. Future studies may build on this work, precharacterizing polychromatic wavefronts and subsequently leveraging this information as *a priori* knowledge for EUV microscopy with chemical sensitivity.

Recent work suggests that multispectral ptychography may be used to characterize both the spatial and spectral structure of attosecond pulses [25]. We have seen in this study that entropy minimization yields DOE designs producing beams with multiple, flux-balanced diffraction orders, which axially coincide upon discrete wavelength changes. Consequently this approach may result in beams with extended depth of focus or even nondiffracting beams when applied to attosecond pulses [44]. However, the influence of our DOEs on the temporal structure of such attosecond pulses has not been investigated, and they may be expected to lead to significant spatiotemporal couplings that are common to diffractive optics [45].

Future challenges are computational in nature: first, while the entropy constraint in the focal plane allowed us to use continuous optimization techniques, the binary constraint imposed on the ZP renders the underlying optimization problem nonconvex. We proposed a heuristic search strategy based on random flips and annealing, which worked for the moderately sized binary ZPs used here but will require more efficient schemes for large-scale focusing optics with orders of magnitude more resolution elements per dimension. This would enable the design of DOEs with larger opening angles and smaller outer zone widths. Similarly, reflective DOEs require larger areas to be optimized but could reach higher efficiencies when used in grazing incidence.

The present work constitutes an approach to polychromatic wavefront sensing that offers orders of magnitude higher lateral resolution than traditional Hartmann–Shack sensors. This may provide new insights into the transfer of aberrations and their spectral dependence in the upconversion of high-harmonic generation [46,47].

Funding. European Research Council (637476); Nederlandse Organisatie voor Wetenschappelijk Onderzoek (13934).

Acknowledgment. The authors thank F. Campi (ARCNL) for useful comments on the manuscript. L.L. gratefully acknowledges the support of NVIDIA Corporation with the donation of the Tesla K40 GPU used for this research.

Disclosures. The authors declare no conflicts of interest.

Supplemental document. See Supplement 1 for supporting content.

[†]These authors contributed equally to this paper.

REFERENCES

1. M. Wieland, C. Spielmann, U. Kleineberg, T. Westerwalbesloh, U. Heinzmann, and T. Wilhein, "Toward time-resolved soft X-ray microscopy using pulsed fs-high-harmonic radiation," Ultramicroscopy **102**, 93–100 (2005).
2. G. Vaschenko, C. Brewer, F. Brizuela, Y. Wang, M. A. Larotonda, B. M. Luther, M. C. Marconi, J. J. Rocca, C. S. Menoni, E. H. Anderson, W. Chao, B. D. Harteneck, J. A. Liddle, Y. Liu, and D. T. Attwood, "Sub-38 nm resolution tabletop microscopy with 13 nm wavelength laser light," Opt. Lett. **31**, 1214–1216 (2006).
3. S. J. Bennett, "Achromatic combinations of hologram optical elements," Appl. Opt. **15**, 542–545 (1976).
4. I. Weingärtner, "Real and achromatic imaging with two planar holographic optical elements," Opt. Commun. **58**, 385–388 (1986).
5. D. Paganin, *Coherent X-Ray Optics*, 1st ed. (Oxford University, 2006).
6. G. S. M. Jansen, X. Liu, K. S. E. Eikema, and S. Witte, "Broadband extreme ultraviolet dispersion measurements using a high-harmonic source," Opt. Lett. **44**, 3625–3628 (2019).

7. J. Miao, P. Charalambous, and J. Kirz, "Extending the methodology of X-ray crystallography to allow imaging of micrometre-sized non-crystalline specimens," Nature **400**, 342–344 (1999).
8. R. L. Sandberg, A. Paul, D. A. Raymondson, S. Hädrich, D. M. Gaudiosi, J. Holtsnider, R. I. Tobey, O. Cohen, M. M. Murnane, H. C. Kapteyn, C. Song, J. Miao, Y. Liu, and F. Salmassi, "Lensless diffractive imaging using tabletop coherent high-harmonic soft-X-ray beams," Phys. Rev. Lett. **99**, 098103 (2007).
9. J. R. Fienup, "Reconstruction of an object from the modulus of its Fourier transform," Opt. Lett. **3**, 27–29 (1978).
10. S. Marchesini, H. He, H. N. Chapman, S. P. Hau-Riege, A. Noy, M. R. Howells, U. Weierstall, and J. C. H. Spence, "X-ray image reconstruction from a diffraction pattern alone," Phys. Rev. B **68**, 140101 (2003).
11. T. Ditmire, E. T. Gumbrell, R. A. Smith, J. W. Tisch, D. D. Meyerhofer, and M. H. Hutchinson, "Spatial coherence measurement of soft x-ray radiation produced by high order harmonic generation," Phys. Rev. Lett. **77**, 4756–4759 (1996).
12. R. Zerne, C. Altucci, M. Bellini, M. B. Gaarde, T. W. Hänsch, A. L'huillier, C. Lyngå, and C. G. Wahlström, "Phase-locked high-order harmonic sources," Phys. Rev. Lett. **79**, 1006–1009 (1997).
13. R. A. Bartels, A. Paul, H. Green, H. C. Kapteyn, M. M. Murnane, S. Backus, I. P. Christov, Y. Liu, D. Attwood, and C. Jacobsen, "Generation of spatially coherent light at extreme ultraviolet wavelengths," Science **297**, 376–378 (2002).
14. B. Abbey, L. W. Whitehead, H. M. Quiney, D. J. Vine, G. A. Cadenazzi, C. A. Henderson, K. A. Nugent, E. Balaur, C. T. Putkunz, A. G. Peele, G. J. Williams, and I. McNulty, "Lensless imaging using broadband X-ray sources," Nat. Photonics **5**, 420–424 (2011).
15. J. Huijts, S. Fernandez, D. Gauthier, M. Kholodtsova, A. Maghraoui, K. Medjoubi, A. Somogyi, W. Boutu, and H. Merdji, "Broadband coherent diffractive imaging," Nat. Photonics **14**, 618–622 (2020).
16. S. Witte, V. T. Tenner, D. W. E. Noom, and K. S. E. Eikema, "Lensless diffractive imaging with ultra-broadband table-top sources: from infrared to extreme-ultraviolet wavelengths," Light. Sci. Appl. **3**, e163 (2014).
17. R. Früke, J. Kutzner, T. Witting, H. Zacharias, and T. Wilhein, "EUV scanning transmission microscope operating with high-harmonic and laser plasma radiation," Europhys. Lett. **72**, 915 (2005).
18. H. Coudert-Alteirac, H. Dacasa, F. Campi, E. Kueny, B. Farkas, F. Brunner, S. Maclot, B. Manschwetus, H. Wikmark, J. Lahl, L. Rading, J. Peschel, B. Major, K. Varjú, G. Dovillaire, P. Zeitoun, P. Johnsson, A. L'Huillier, and P. Rudawski, "Micro-focusing of broadband high-order harmonic radiation by a double toroidal mirror," Appl. Sci. **7**, 1159 (2017).
19. J. M. Rodenburg and H. M. L. Faulkner, "A phase retrieval algorithm for shifting illumination," Appl. Phys. Lett. **85**, 4795–4797 (2004).
20. J. Rodenburg and A. Maiden, "Ptychography," in *Springer Handbook of Microscopy* (Springer, 2019), p. 2.
21. P. Thibault, M. Dierolf, A. Menzel, O. Bunk, C. David, and F. Pfeiffer, "High-resolution scanning X-ray diffraction microscopy," Science **321**, 379–382 (2008).
22. M. D. Seaberg, B. Zhang, D. F. Gardner, E. R. Shanblatt, M. M. Murnane, H. C. Kapteyn, and D. E. Adams, "Tabletop nanometer extreme ultraviolet imaging in an extended reflection mode using coherent Fresnel ptychography," Optica **1**, 39–44 (2014).
23. M. Du, L. Loetgering, K. Eikema, and S. Witte, "Measuring laser beam quality, wavefronts, and lens aberrations using ptychography," Opt. Express **28**, 5022–5034 (2020).
24. D. J. Batey, D. Claus, and J. M. Rodenburg, "Information multiplexing in ptychography," Ultramicroscopy **138**, 13–21 (2014).
25. A. Rana, J. Zhang, M. Pham, A. Yuan, Y. H. Lo, H. Jiang, S. J. Osher, and J. Miao, "Potential of attosecond coherent diffractive imaging," Phys. Rev. Lett. **125**, 086101 (2020).
26. P. D. Baksh, M. Odstrčil, H.-S. Kim, S. A. Boden, J. G. Frey, and W. S. Brocklesby, "Wide-field broadband extreme ultraviolet transmission ptychography using a high-harmonic source," Opt. Lett. **41**, 1317–1320 (2016).
27. C. L. Porter, M. Tanksalvala, M. Gerrity, G. Miley, X. Zhang, C. Bevis, E. Shanblatt, R. Karl, M. M. Murnane, D. E. Adams, and H. C. Kapteyn, "General-purpose, wide field-of-view reflection imaging with a tabletop 13 nm light source," Optica **4**, 1552–1557 (2017).
28. J. Rothhardt, G. K. Tadesse, W. Eschen, and J. Limpert, "Table-top nanoscale coherent imaging with XUV light," J. Opt. **20**, 113001 (2018).
29. G. K. Tadesse, W. Eschen, R. Klas, M. Tschernajew, F. Tuitje, M. Steinert, M. Zilk, V. Schuster, M. Zürch, T. Pertsch, C. Spielmann, J. Limpert, and J. Rothhardt, "Wavelength-scale ptychographic coherent diffractive imaging using a high-order harmonic source," Sci. Rep. **9**, 1735 (2019).
30. P. D. Baksh, M. Ostrčil, M. Miszczak, C. Pooley, R. T. Chapman, A. S. Wyatt, E. Springate, J. E. Chad, K. Deinhardt, J. G. Frey, and W. S. Brocklesby, "Quantitative and correlative extreme ultraviolet coherent imaging of mouse hippocampal neurons at high resolution," Sci. Adv. **6**, eaaz3025 (2020).
31. B. Zhang, D. F. Gardner, M. H. Seaberg, E. R. Shanblatt, C. L. Porter, R. Karl, C. A. Mancuso, H. C. Kapteyn, M. M. Murnane, and D. E. Adams, "Ptychographic hyperspectral spectromicroscopy with an extreme ultraviolet high harmonic comb," Opt. Express **24**, 18745–18754 (2016).
32. A. M. Maiden, M. J. Humphry, F. Zhang, and J. M. Rodenburg, "Superresolution imaging via ptychography," J. Opt. Soc. Am. A **28**, 604–612 (2011).
33. M. Guizar-Sicairos, M. Holler, A. Diaz, J. Vila-Comamala, O. Bunk, and A. Menzel, "Role of the illumination spatial-frequency spectrum for ptychography," Phys. Rev. B **86**, 100103 (2012).
34. M. Odstrčil, M. Lebugle, M. Guizar-Sicairos, C. David, and M. Holler, "Towards optimized illumination for high-resolution ptychography," Opt. Express **27**, 14981–14997 (2019).
35. L. Loetgering, M. Baluktsian, K. Keskinbora, R. Horstmeyer, T. Wilhein, G. Schütz, K. S. E. Eikema, and S. Witte, "Generation and characterization of focused helical X-ray beams," Sci. Adv. **6**, eaax8836 (2020).
36. R. B. Ash, *Information Theory*, 1st ed. (Dover, 1990).
37. K. Kreutz-Delgado, "The complex gradient operator and the CR-calculus," arXiv:0906.4835 (2009).
38. K. Matsushima and T. Shimobaba, "Band-limited angular spectrum method for numerical simulation of free-space propagation in far and near fields," Opt. Express **17**, 19662–19673 (2009).
39. J. W. Goodman, *Introduction to Fourier Optics*, 4th ed. (WH Freeman, 2017).
40. J. Miao, D. Sayre, and H. N. Chapman, "Phase retrieval from the magnitude of the Fourier transforms of nonperiodic objects," J. Opt. Soc. Am. A **15**, 1662–1669 (1998).
41. L. Freisem, G. S. M. Jansen, D. Rudolf, K. S. E. Eikema, and S. Witte, "Spectrally resolved single-shot wavefront sensing of broadband high-harmonic sources," Opt. Express **26**, 6860–6871 (2018).
42. F. Tuitje, W. Eschen, G. K. Tadesse, J. Limpert, J. Rothhardt, and C. Spielmann, "Reliability of ptychography on periodic structures," OSA Contin. **3**, 1691–1702 (2020).
43. O. Bunk, M. Dierolf, S. Kynde, I. Johnson, O. Marti, and F. Pfeiffer, "Influence of the overlap parameter on the convergence of the ptychographical iterative engine," Ultramicroscopy **108**, 481–487 (2008).
44. J. Durnin, "Exact solutions for nondiffracting beams. I. The scalar theory," J. Opt. Soc. Am. A **4**, 651–654 (1987).
45. S. Akturk, X. Gu, P. Bowlan, and R. Trebino, "Spatio-temporal couplings in ultrashort laser pulses," J. Opt. **12**, 093001 (2010).
46. H. Wikmark, C. Guo, J. Vogelsang, P. W. Smorenburg, H. Coudert-Alteirac, J. Lahl, J. Peschel, P. Rudawski, H. Dacasa, S. Carlström, S. MacLot, M. B. Gaarde, P. Johnsson, C. L. Arnold, and A. L'Huillier, "Spatiotemporal coupling of attosecond pulses," Proc. Natl. Acad. Sci. USA **116**, 4779–4787 (2019).
47. H. Dacasa, H. Coudert-Alteirac, C. Guo, E. Kueny, F. Campi, J. Lahl, J. Peschel, H. Wikmark, B. Major, E. Malm, D. Alj, K. Varjú, C. L. Arnold, G. Dovillaire, P. Johnsson, A. L'Huillier, S. Maclot, P. Rudawski, and P. Zeitoun, "Single-shot extreme-ultraviolet wavefront measurements of high-order harmonics," Opt. Express **27**, 2656–2670 (2019).